Hybrid DEM-FDM Modelling of Railway Track Performance

Nohemí Olivera and Juan Manuel Mayoral *

Posted Date: 2 March 2026

doi: 10.20944/preprints202602.2004.v1

Keywords: performance; railways; cyclic; breakage; ballast; factor of safety

 doi:10.20944/preprints202602.2004.v1

Article

Hybrid DEM-FDM Modelling of Railway Track Performance

Nohemí Olivera and Juan Manuel Mayoral *

Geotechnical Department, Institute of Engineering, National University of Mexico, Mexico City 04510, Mexico

* Correspondence: jmayoralv@iingen.unam.mx

Abstract

The performance of ballasted railway tracks under cyclic loading is a critical issue in urban railway systems, where high traffic frequency and geometric constraints accelerate track degradation, which, in turn, leads to accumulation of plastic deformations that potentially reduce operation efficiency. This study presents a numerical framework for rail track performance assessment based on two complementary modeling approaches: a fully continuous Finite Difference Method (FDM) model, and a hybrid Discrete Element Method–Finite Difference Method (DEM–FDM) model. The continuous FDM simulations are employed to evaluate the global mechanical response of the track support system and to compute conventional stability indicators, including the factor of safety (FS). In parallel, the hybrid DEM–FDM simulations explicitly represent the ballast layer using DEM to capture inter-particle interactions, accumulation of permanent deformation, and particle fragmentation under cyclic loading, while rails, sleepers, sub-ballast, and subgrade are modeled using FDM to describe system-level load transfer. Ballast performance is assessed by linking safety factors obtained from the continuous models with mechanically derived permanent deformation and stress measures extracted from the hybrid simulations. This dual-modeling framework enables a systematic investigation of the influence of ballast layer thickness and material type on deformation accumulation, stress transmission, and granular degradation mechanisms. The results reveal distinct behavioral trends among different ballast materials, showing that increased ballast thickness generally improves track performance, while material-specific degradation mechanisms govern the evolution of permanent deformation under repeated loading. The proposed approach establishes a quantitative bridge between traditional stability-based design metrics and deformation-based performance indicators, providing a rational basis for performance-based evaluation, comparison, and optimization of ballast configurations, through a set of robust numerically derived relationships for railway track design abstract should be an objective representation of the article and it must not contain results that are not presented and substantiated in the main text and should not exaggerate the main conclusions.

Keywords: performance; railways; cyclic; breakage; ballast; factor of safety

1. Introduction

Ballast is the primary granular component in conventional railway systems, and its structural function is critical to efficient load transmission, track geometry stability, and adequate dynamic performance under repeated traffic. Due to its granular nature, ballast is susceptible to several degradation mechanisms, including permanent strain, particle breakage and rearrangement, abrasion, and fracture. These processes lead to stiffness degradation, differential settlement, and recurrent maintenance requirements [1,2].

In urban railway systems, ballast degradation is further intensified by high travel frequency, dynamic effects from stopping and acceleration, and geometric constraints that limit the height of the track support layers [3,4]. Unlike high-speed railway lines, where train speed is often the dominant parameter, urban tracks are characterized by axle loads, high loading frequency, and relatively low

 doi:10.20944/preprints202602.2004.v1

confinement. This combination produces complex degradation patterns, in which ballast becomes the governing component controlling track deformation and long-term performance. Experimental and numerical studies have shown that ballast response under cyclic loading is highly sensitive to intrinsic material properties, such as mineralogy, particle angularity, and particle size distribution [5,6], as well as to operational variables, including load amplitude, train speed, and lateral confinement [4,7]. Despite these advances, traditional design methods are still unable to predict permanent deformation and degradation under repeated loading, primarily because granular materials are strongly nonlinear and history-dependent, and because particle breakage plays an explicit role.

In this context, numerical approaches based on the Discrete Element Method (DEM) have become powerful tools for investigating ballast performance, as they allow explicit modeling of interparticle contacts, force-chain development, plastic deformation, and particle fragmentation. Moreover, coupled DEM–continuum approaches, such as DEM–FEM and DEM–FDM formulations, enable the interaction between the ballast layer and the underlying sub-ballast and subgrade to be captured, leading to a more realistic representation of stress redistribution and system-level response [8–10].

Nevertheless, important gaps remain in the quantitative assessment of the combined effects of ballast height, material type, loading magnitude, and operating speed on accumulated deformation, particle breakage, and overall track stability. In particular, there is limited evidence linking these variables to performance-based design criteria defined by deformation limits and safety factors, especially for urban railway applications.

This paper presents a novel approach to evaluate the response to rolling stock cyclic loading effects on rail tract support, incorporating the safety factor, accumulated deformations, and stability of a railway system through hybrid DEM–FDM numerical models that explicitly represent plastic deformation, particle breakage, and stress redistribution between layers. Simultaneously, fully continuous finite difference models were developed to obtain safety factors using the traditional method. The study focuses on: (i) comparing the performance of different ballast materials (basalt, granite, and limestone), (ii) assessing the influence of ballast layer height (0.25, 0.35, and 0.40 m), and (iii) evaluating the results in terms of the safety factor. The results reveal several behavioral trends among the ballast materials, showing that greater ballast thickness generally improves track performance, while specific degradation mechanisms determine the evolution of permanent deformation under repeated loading. The equations derived provide a valuable conceptual framework and a quantitative starting point for integrating deformation monitoring into ballast stability assessment. The findings are directly applicable to urban railway systems, where geometric constraints, cyclic loads, and operational speeds require design approaches that control deformation and extend the service life of the track support structure.

2. Methodology

In modern rail track design, railway ballast performance under dynamic loading is a key issue, which must be established to properly assess track durability, establish maintenance programs, and ensure safety in both urban and inter-urban railway track systems. The interaction among the rail, sleeper, and ballast layers governs permanent settlement, track geometry stability, and the overall support structural response, particularly under repeated loading from frequent train passages. Ballast exhibits a highly nonlinear mechanical response during rolling stock constant operation. Changes in stiffness and progressive softening depend on loading history, granular geometry arrangement, confinement conditions, and particle degradation. Under cyclic loading, ballast behavior passes through several response stages: shakedown, ratcheting, and plastic collapse. These stages determine whether permanent deformations stabilize or continue accumulating with increasing load cycles. Thus, their characterization is essential for assessing track durability and maintenance requirements.

 doi:10.20944/preprints202602.2004.v1

In conventional practice, the design of the railway track support system is based on an implicit imposed factor of safety, neglecting the importance of establishing the expected plastic deformation accumulation properly, as summarized in Table 1.

Table 1. Design criteria for railway track support.

Norm / Method	Main design criterion	Value / Key parameter	Implicit or recommended Factor of safety (FS)
AREMA (EE. UU.) [11]	Allowable pressure	• Ballast: 448-586 kPa (65-85 psi) under the sleeper. • Subgrade: 124 kPa (18 psi).	FS = 2 (for subgrade)
European Standards (EN + National) [12,13]	1. Bearing capacity (allowable stress)	Allowable vertical stress (σ_{adm}): Varies with the type of soil.	FS global typical = 1.5.
	2. Ballast Module (k)	Minimum values of k (MN/m^3).	Included in the requirement of a high minimum value.
UIC 719 R [14]	Bearing capacity / Strain	Static pressure under sleeper (q): e.g., q = 500 kPa for conventional tracks.	-
JR (Japan) – WJR [15]	Allowable Pressure in Subgrade	288 kPa (2.9 kgf/cm^2) for lines with mixed traffic.	FS high (estimated >3). Based on performance under extreme dynamic loads and fatigue cycles.
Network Rail (UK) [16]	Support Capacity / CBR	Minimum CBR of improved subgrade: = 5% (static), = 15% (dynamic).	Included in the specified minimum values, which far exceed the failure thresholds.
Li & Selig (Analytical Method) [17]	Permanent strain	Cyclic effort in subgrade (σc) to limit settlement to a threshold (e.g., 25 mm) after N cycles.	It is designed so that the accumulated deformation after the service life does not exceed the allowable limit.

To establish a quantitative relationship between the factor of safety and the permanent strain (ε_p), a numerical investigation was conducted to evaluate the development of permanent deformation within the track support system. A parallel modeling strategy was adopted, combining a hybrid DEM–FDM approach with a conventional continuum model based on the finite difference method, for several rail track support configurations with varying granular layer thicknesses. Figure 1 depicts the methodology employed.

 doi:10.20944/preprints202602.2004.v1

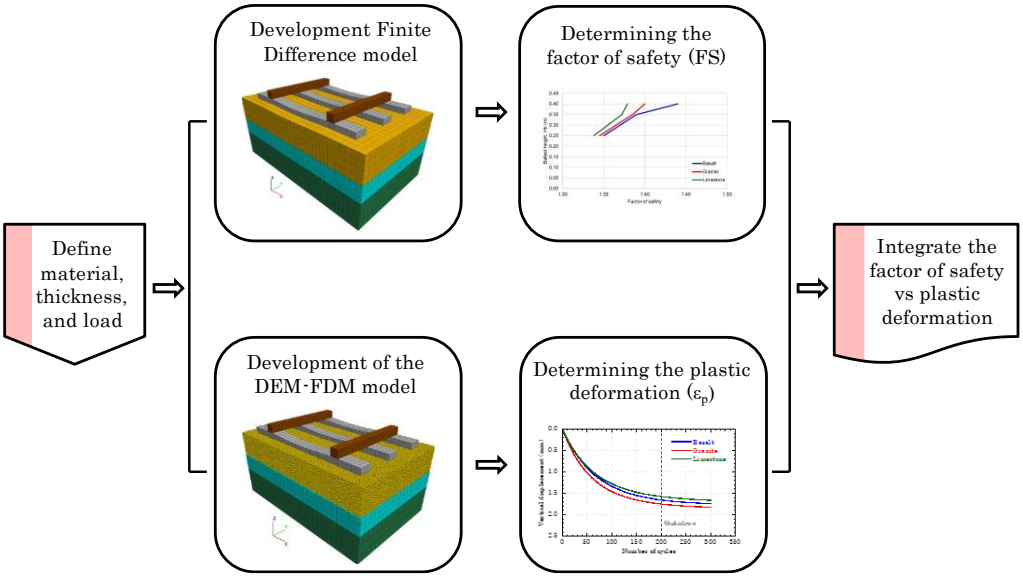

Figure 1. Schematic representation of the proposed methodology.

3. Numerical Modelling

The numerical models implemented in this study, namely the finite difference models (FDM) and the DEM–FDM hybrid models, are schematically illustrated in Figure 2. The following sections provide a comprehensive description of the modeling criteria adopted for both approaches, including geometric definitions, assigned material properties, boundary conditions, particle generation, calibration within the DEM framework, and the particle breakage criterion used in the hybrid models.

3.1. Hybrid DEM-FDM Model

Three-dimensional coupled numerical models were developed using the finite-difference method (FDM) in FLAC^{3D} and the discrete element method (DEM) in PFC^{3D} (Particle Flow Code 3D) [18]. The contact model parameters used in the coupled analyses were obtained from a prior calibration against triaxial test simulations as follows. The triaxial test used for calibration was taken from technical literature. Parameter values were determined through an iterative procedure to ensure that the calibrated contact properties provided an adequate representation of ballast mechanical behavior within the coupled DEM–FDM framework.

3.2. Particle Contact Model

For the hybrid model, particle contact was modeled using the linear rolling resistance (RRLM) model, implemented in the discrete element software PFC^{3D}, which extends classical contact formulations to capture dissipative mechanisms associated with relative rotational motion between particles and between particles and boundaries. Although often neglected in simplified modeling approaches, rolling resistance plays a key role in granular materials, where micro-scale surface roughness, irreversible contact deformations, and non-spherical particle geometry generate additional rolling resistance [19,20].

The model is formulated within an independent elasto-plastic framework that operates in parallel with and is weakly coupled to the contact law governing normal and tangential forces [18]. Its implementation introduces a resisting contact moment M_r acting at the interaction plane, which opposes the relative rotational displacement θ_r between the contacting entities.

Two primary internal variables are defined: the elastic component of the relative rotational displacement, θ_r, and the accumulated plastic component, θ_r^{pl}. The kinematic relationship is expressed through an additive decomposition,

 doi:10.20944/preprints202602.2004.v1

$$\theta_r = \theta_r^t - \theta_r^{pl} \quad (1)$$

where θ_r^t denotes the total incremental relative rotational displacement, computed from the difference in angular velocities, ω_A and ω_B, of the contacting entities (A and B) over a time increment Δt,

$$\Delta\theta_r^t = (\omega_B - \omega_A) \times \Delta t \quad (2)$$

The elastic response of the rolling resistance model is defined through an isotropic rotational stiffness tensor. In its general form, this tensor is represented by a second-order identity tensor scaled by the rolling stiffness parameter k_r, such that the elastic rolling moment is given by

$$M_r^e = -K_r : \theta_r = k_r \cdot \mathrm{I} : \theta_r \quad (3)$$

where I is the second-order identity tensor. In the simplified scalar implementation adopted in this study, the rolling moment depends solely on the magnitude of the relative rotational displacement

3.3. Particle Contact Model

To simulate ballast particle breakage under static and cyclic loading, the non–mass-conservative multigenerational fragmentation criterion proposed by Ciantia et al. [21] was adopted. This approach combines an elastoplastic breakage criterion based on the theory of Russell and Muir Wood [22] with a controlled spawning procedure, enabling progressive material degradation to be modeled without prohibitive computational costs.

The implemented criterion establishes that a particle breaks when the mobilized strength, κ_{mob}, exceeds the intrinsic strength of the material κ.

$$M_r^e = -K_r : \theta_r = k_r \cdot \mathrm{I} : \theta_r \quad (4)$$

where κ is derived from the uniaxial compressive (σ_c) and tensile strengths (σ_t) of the particle material. The mobilized strength is computed as:

$$M_r^e = -K_r : \theta_r = k_r \cdot \mathrm{I} : \theta_r \quad (5)$$

where F is the maximum normal contact force, R is the particle radius, υ is Poisson's ratio, $\chi = |\sigma_c|/\sigma_t - 1$ is a microstructural parameter, and θ_0 is the contact semi-angle, which in the present model is determined using Hertzian contact theory.

A Weibull-type scaling law was introduced to model the dependence of particle strength on particle size:

$$M_r^e = -K_r : \theta_r = k_r \cdot \mathrm{I} : \theta_r \quad (6)$$

where $\sigma_{\mathrm{lim},0}$ is the reference crushing strength associated with a characteristic diameter d_0, and m is the Weibull modulus controlling the sensitivity of strength to particle size [23].

When the breakage criterion is satisfied, the original particle is replaced by a fixed configuration of 14 inscribed, mutually tangent spheres, whose relative positions are rotated to align with the direction of the critical contact force (Figure 3). This arrangement minimizes volume loss and reproduces fracture patterns similar to those observed experimentally in granular materials subjected to diametral compression.

 doi:10.20944/preprints202602.2004.v1

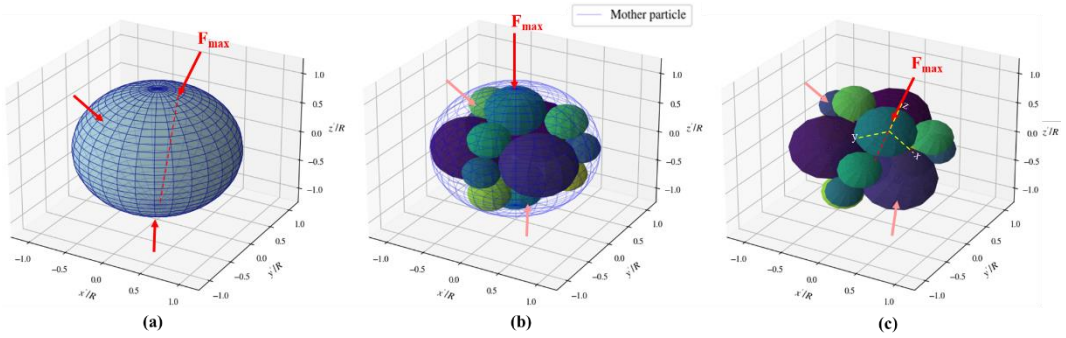

Figure 3. The particle breakage configuration, modified from Ciantia et al. [21].

Unlike other multigenerational approaches, the model does not conserve mass within the mechanical system, assuming that the lost mass corresponds to fine particles that do not significantly contribute to force transmission. Nevertheless, for comparison with particle size distribution tests, the excluded mass is redistributed externally according to a fractal distribution with a dimension alpha of 0.6, as suggested by Einav [24], and validated by Ciantia et al. [21]. To control the exponential growth in the number of particles, a fragmentation limit, $d_{limit} = 0.55 \cdot d_{50}$, was defined below which particles are no longer allowed to break. A schematic of the adopted breakage criterion and its implementation in the DEM framework is shown in Figure 4.

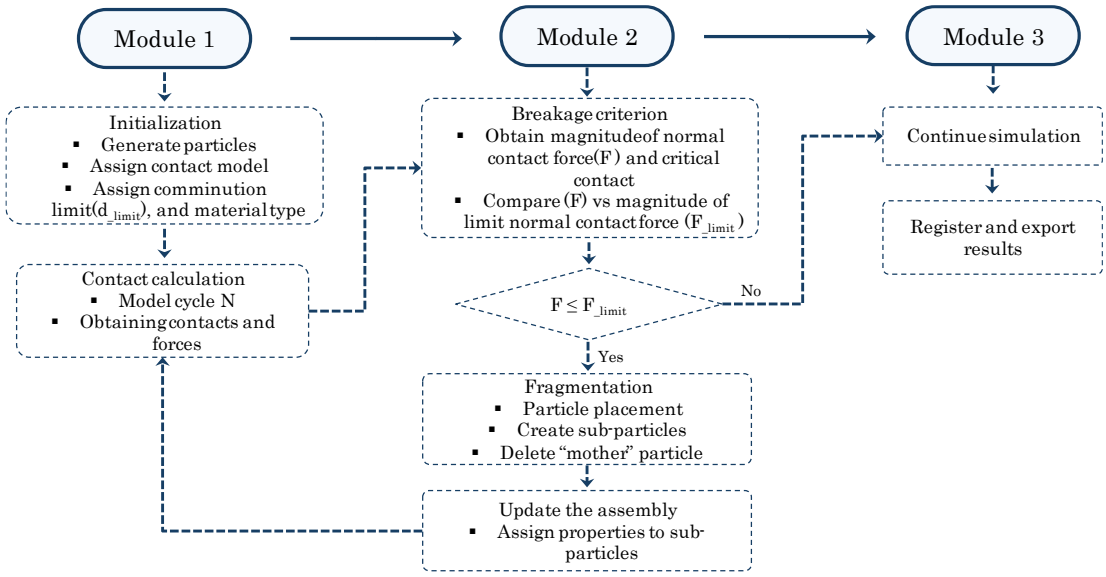

Figure 4. Schematic diagram of the ballast breakage criterion implemented in DEM.

3.4. Numerical Hybrid Modelling Boundary Conditions

Periodic boundary conditions were applied to the numerical domain. When the ball centroid falls outside of the model domain, they are translated back to the opposite side of the model. To ensure that contacts are created as if the model were continuous, "ghost" balls are introduced. To optimize computational efficiency while maintaining a representative track configuration, three sleepers were modeled with a spacing of 0.60 m. The numerical model has a longitudinal length of 1.80 m, a transverse width of 2.80 m, and a variable height depending on the selected ballast height. The overall model geometry and dimensions are shown in Figure 5.

 doi:10.20944/preprints202602.2004.v1

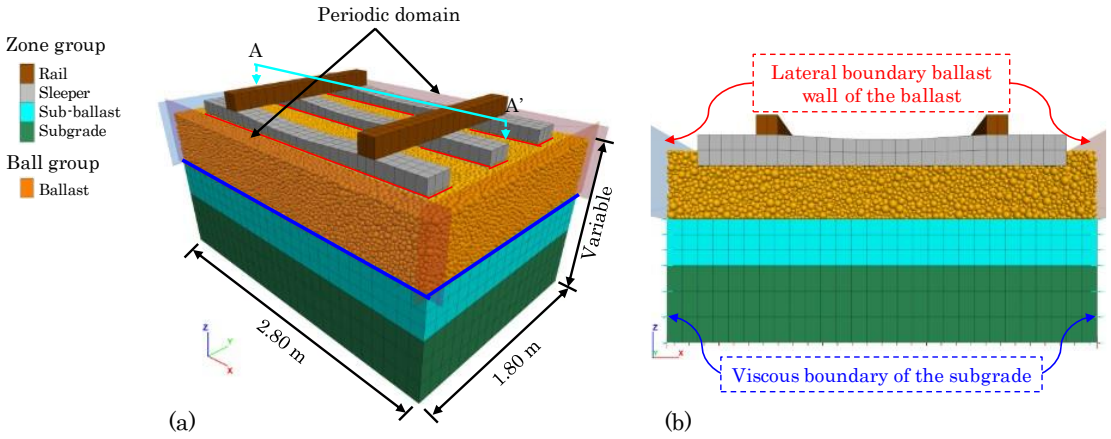

Figure 5. Dimensions and domain of the coupled model.

To evaluate the mechanical behavior of all track layers, a hybrid DEM–FDM numerical model was developed, as illustrated in Figure 6. The subgrade, base layer, sleepers, and rail were modeled using the finite difference method (FDM), whereas the ballast layer was simulated using the discrete element method (DEM). Interactions between ballast particles and the base layer, as well as between ballast and sleepers, were represented through interface elements generated at the contact zone between the continuous and discrete domains.

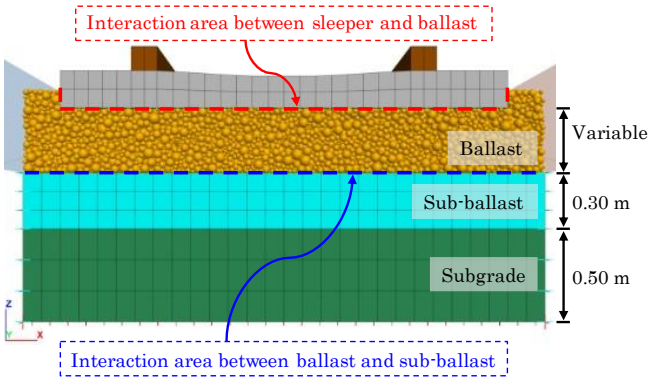

Figure 6. Interaction between the continuous and discrete domain regions.

Because ballast aggregates are highly heterogeneous, their mechanical response cannot be fully interpreted using conventional continuum parameters such as stress and strain alone. For this reason, internal responses within the ballast layer were observed using measurement spheres available in PFC^{3D} [18]. To obtain stress distributions within the ballast bed, measurement spheres were generated to capture the average stress and strain in the ballast layer, as shown in Figure 7.

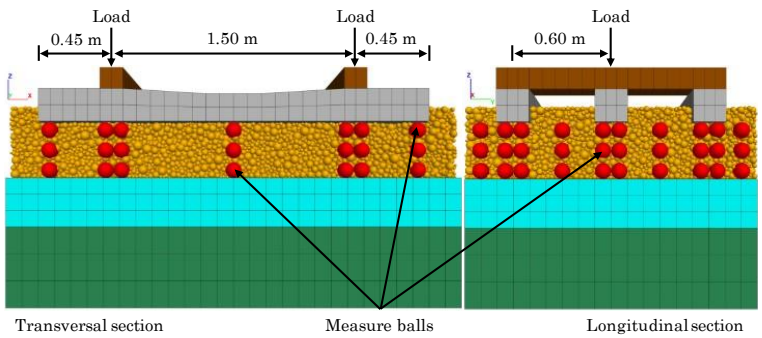

Figure 7. Location of measurement spheres within the ballast layer.

 doi:10.20944/preprints202602.2004.v1

3.5. Model Calibration

The model calibration was based on extensively documented and validated experimental results from the technical literature [25–27], derived from carefully selected large-scale triaxial tests. These studies are in good agreement with the recommended properties for materials often used in railway track supports. Thus, these data were deemed appropriate for this initial research phase. While the importance of direct experimental validation is acknowledged, the data allows for establishing the soundness of the proposed methodology.

The properties of the materials evaluated in this study (basalt, granite, and limestone) are summarized in Table 2. Figure 8 shows the particle-size distribution of each material, determined by sieve analysis in accordance with ASTM C136/C136M-19 [28]. In the numerical models, ballast particles were randomly generated in the longitudinal and vertical directions within the specified domain, reproducing the target ballast size distribution.

Table 2. Characteristics of material.

Material	Density ρ	Uniformity Coefficient, C_u	Coefficient of Curvature, C_c	D_{max} (mm)	D_{min} (mm)
Basalt	2.60	1.48	0.99	53	13
Granite	2.68	1.52	0.90	63	16
Limestone	2.65	1.46	0.97	63	13

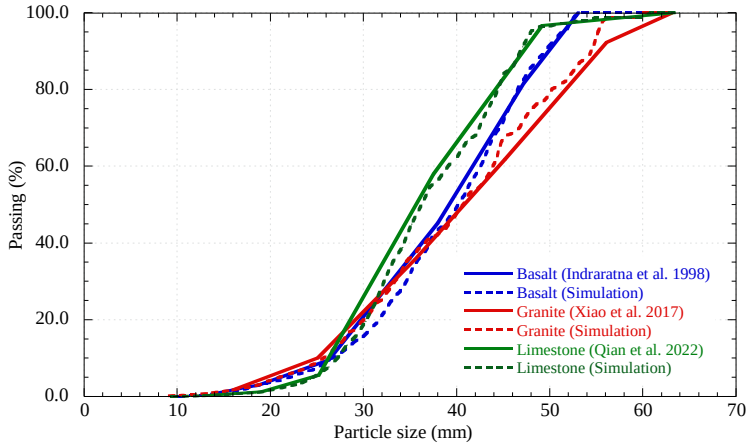

Figure 8. Particle size distribution of materials used in numerical models.

For calibration, large-scale triaxial tests previously reported by various authors [25–27] were reproduced numerically. Each simulation was designed to match the laboratory configurations described in those studies, ensuring that the numerical response could be directly compared with the experimental results.

Triaxial tests were conducted using cylindrical specimens of varying sizes and a grain-size distribution corresponding to previous experimental data reported in Indraratna et al. [25], Xiao et al. [26], and Qian et al. [27]. Each specimen, enclosed by two flat plates and a curved wall (Figure 9), was created by randomly placing ballast particles and adjusting the friction coefficient to achieve dense or loose packing depending on the case considered. Isotropic confinement was applied using the PFC^{3D} servo-control algorithm until the target pressure was reached.

 doi:10.20944/preprints202602.2004.v1

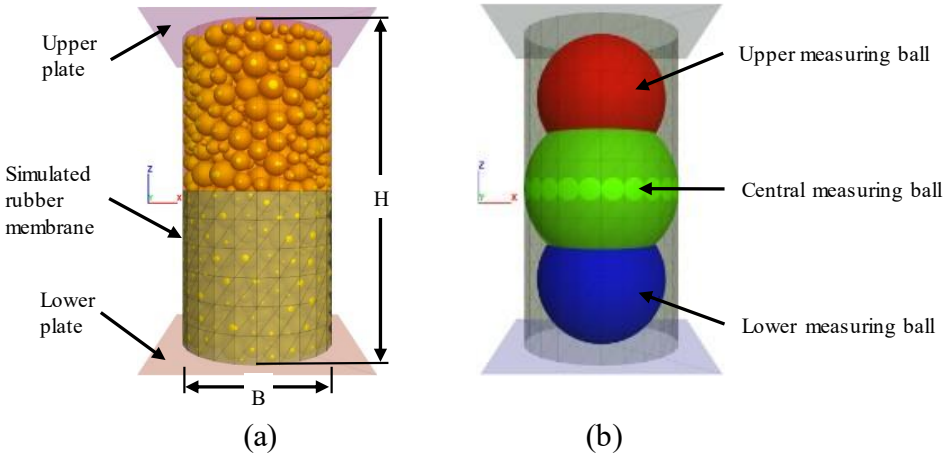

Figure 9. Numerical triaxial model (a) general characteristics and (b) measure balls.

After the sample was obtained, a monotonic triaxial test was conducted by controlling axial deformation and maintaining constant lateral pressure. During loading, deviatoric stress and axial deformation were recorded, and measurement spheres were used to assess particle breakage.

Because obtaining DEM simulation parameters directly from experimental results is complex, most researchers have historically determined these parameters using indirect methods described below and adopted in this study. In the first stage, a comprehensive literature review was conducted to establish reasonable parameter value ranges. Subsequently, these values were optimized through trial-and-error iterations to align the simulated macroscopic mechanical behavior with available experimental data. The final parameters used in the DEM simulations are specified in Table 3.

Table 3. Parameters used on the DEM models.

Material	Density of ballast particles (kg/m³)	Normal Stiffness, k_n (N/m)	Shear Stiffness, k_s (N/m)	Damping coefficient -	Friction Coefficient, μ -	Rolling Friction Coefficient, μ_r -
Basalt	2650	2×10^6	2×10^6	0.7	0.4	0.8
Granite	2680	3×10^8	3×10^8	0.7	0.5	0.6
Limestone	2600	2×10^7	2×10^7	0.7	0.5	0.7

Figure 10 compares the computed and measured responses after the final trial of the calibration process. The numerical response satisfactorily reproduces the behavior observed in large-scale triaxial tests, demonstrating adequate correspondence between the stress–strain curves across the different confining stress levels.

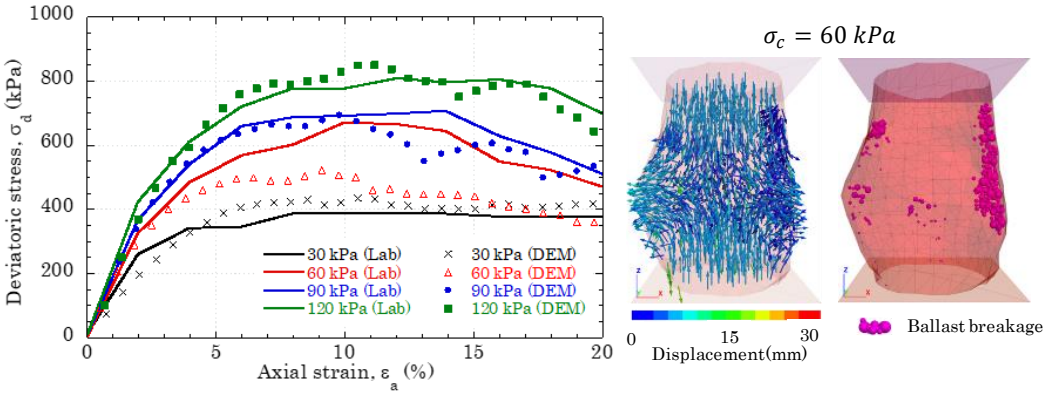

(**a**) Basalt

 doi:10.20944/preprints202602.2004.v1

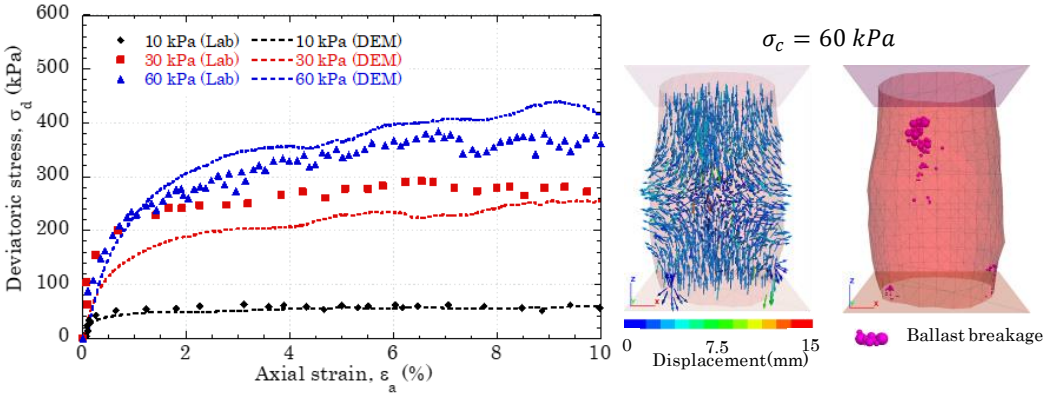

(**b**) Granite

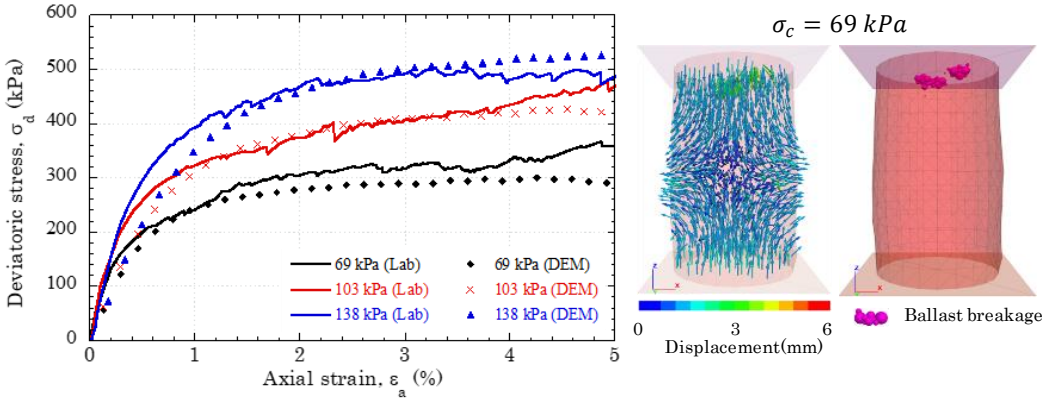

(**c**) Limestone

Figure 10. Comparison of numerical and experimental stress–strain curves, particle breakage patterns in triaxial specimens, and displacement vectors under different confining stresses.

Based on the model calibration, the normal stiffness (k_n) and tangential stiffness (k_s) were found to have the greatest influence on the model's response, as they directly control the initial slope of the stress–strain curve. When these values are high, the material exhibits a more brittle behavior, reaching its peak strength too early. Conversely, friction mainly controls the maximum strength of the assembly, while rolling resistance determines the shape of the curve in the post-peak stage, defining the transition between the maximum load state and the residual condition.

Given the critical importance of ballast compaction conditions in numerical simulations to properly establish the initial stresses, this study adopted a multilayer compaction procedure proposed by various researchers [8,29,30], as illustrated in Figure 9. The compaction process initiates with three ballast layers, with compaction pressures exceeding 200 kPa applied at each stage. After each compaction iteration, excess particles were removed, and auxiliary surfaces generated. The compaction procedure was subsequently reiterated to ensure adequate particle densification. Ultimately, the sleepers and rails were positioned on the compacted ballast layer, following which the auxiliary surfaces were removed.

Sub-ballast and subgrade were modeled using a perfectly elastoplastic formulation governed by the Mohr–Coulomb yield criterion. At the same time, the rail and sleeper were assumed to behave elastically. The material properties considered in the numerical model are summarized in Table 4.

 doi:10.20944/preprints202602.2004.v1

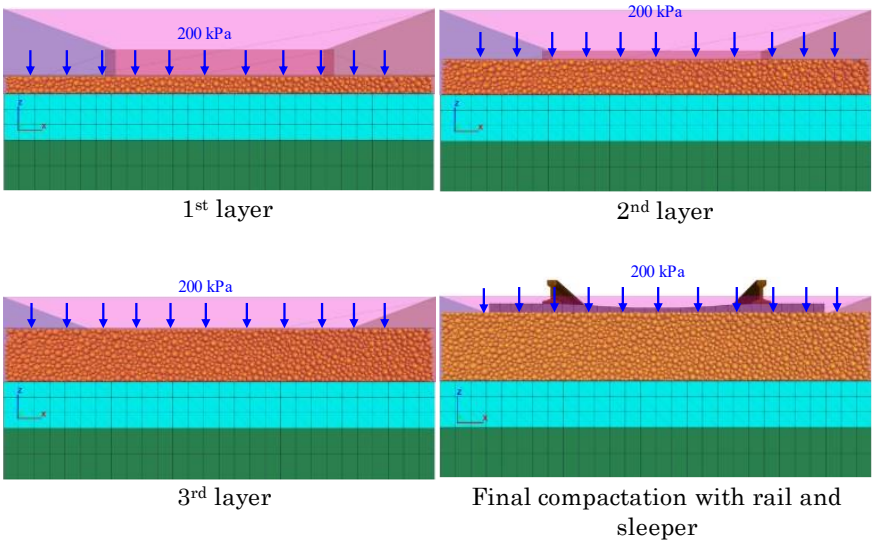

Figure 11. Multilayer ballast compaction procedure.

Table 4. Properties of the continuous model [31].

Group	Constitutive Model	γ (kN/m³)	c (MPa)	ϕ (°)	E (MPa)	ν (-)
Rail	Elastic	79.0	-	-	210000	0.30
Sleeper	Elastic	24.0	-	-	47500	0.18
Sub-ballast	Mohr-Coulomb	17.6	0	43	143	0.35
Subgrade	Mohr-Coulomb	18.8	0.03	35	60	0.35

3.6. Train Load Considered

To simulate the loads transmitted by the bogie, an axle load of 147.15 kPa (73.58 kPa per wheel) was considered. Additionally, a dynamic impact factor (IF) was incorporated using Equation (7) [11], which accounts for a percentage increase in vertical load to represent the dynamic effects of wheel-rail irregularities.

$$IF = \frac{33V}{100D} \tag{7}$$

With a design speed of 85 km/h (52.8 mph) and a wheel diameter of 0.91 m (35.98 in), an impact factor of 0.48 was obtained. For all cases analyzed, the same wheel load (see Table 5) was applied to the central sleeper.

Table 5. Wheel load was adopted in the analyses.

Load per axle (kPa)	Load per wheel (kPa)	Impact Factor, IF	Load per Wheel with IF (kPa)
147.15	73.58	0.48	108.89

Thus, the cyclic load was applied 300 times with a frequency of 10 Hz, considering a distance between each axle of 2.40 m. The loading and boundary conditions described above were consistently applied to all numerical models included in the parametric analysis. In this study, only the ballast layer height was varied, with values of 0.25 m, 0.35 m, and 0.40 m corresponding to Cases I, II, and III, respectively, as shown in Figure 12.

 doi:10.20944/preprints202602.2004.v1

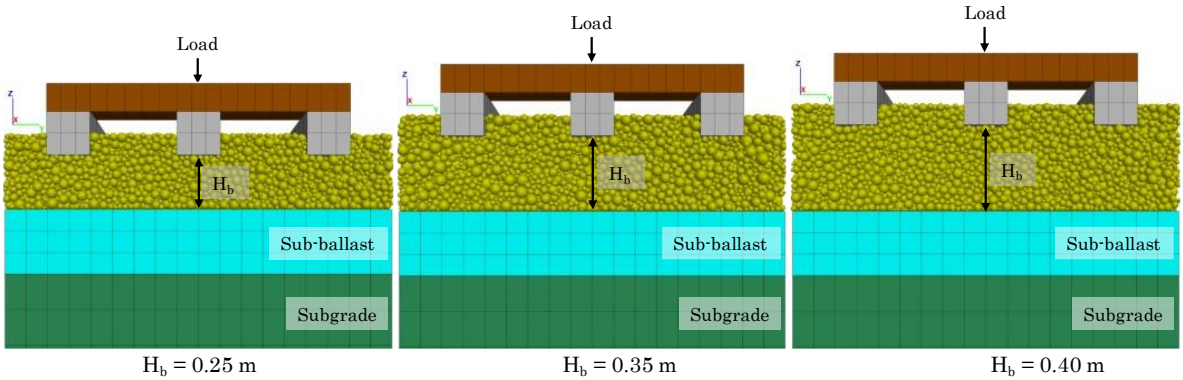

Figure 12. Parametric study cases with varying ballast layer height.

3.7. Finite Differences Model

In parallel with the hybrid models, three-dimensional finite-difference numerical models were developed in FLAC^{3D} to assess the ballast's safety factor following a conventional practice-oriented method. The geometric configuration is shown in Figure 13. To ensure comparability of results, the parametric analyses of the finite difference models faithfully replicated the variables studied in the hybrid models: material types (basalt, granite, limestone), ballast thicknesses, and applied loading conditions. In these models, the behavior of the geomaterials was represented using an elastoplastic constitutive law with a Mohr–Coulomb failure criterion. Although this constitutive model simplify the stress-strain relationship of the geomaterials, it is still used frequently in engineering practice. For completeness, a more robust model was also used for comparison purposes.

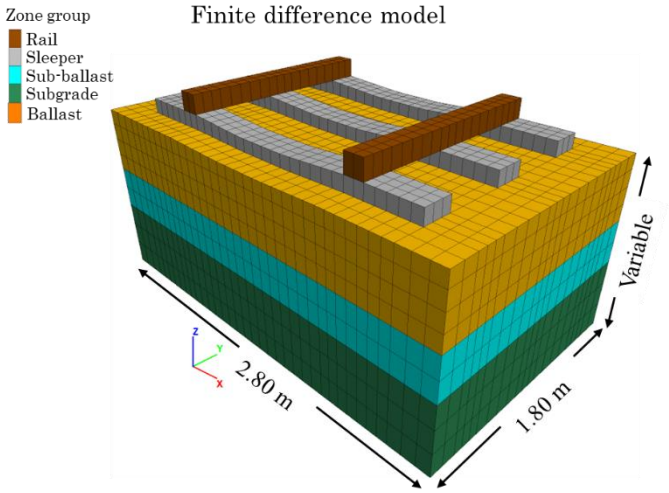

Figure 13. Representation of the numerical finite-difference model.

The geotechnical parameters used in this study, such as unit weight, friction angle, Young's modulus, and Poisson's ratio, have been derived from experimental data reported in specialized literature, particularly from large-scale triaxial tests conducted with limestone and granite ballast under static and cyclic conditions [25–27] and summarized in Table 6. The unit weight (γ) values were obtained directly from laboratory measurements, while the friction angle (ϕ) was calculated from Mohr-Coulomb envelopes under different confining pressures. It was assumed that cohesion was insignificant, in line with the granular nature of the ballast. Young's modulus (E) was estimated from the initial slopes of the stress-strain curves, and Poisson's ratio (υ) was taken from typical values for granular materials under drained conditions. In all cases, consistency has been maintained with

 doi:10.20944/preprints202602.2004.v1

the drained and cohesionless behavior characteristic of ballast, ensuring that the parameter selection is supported by widely validated experimental evidence.

Table 6. Parameters for ballast materials adopted in the continuum (FDM) numerical models.

Material	γ (kN/m³)	c (MPa)	ϕ (°)	E (MPa)	υ (-)
Basalt	15.3	0	53	200	0.30
Granite	15.7	0	54	240	0.25
Limestone	16.0	0	45	150	0.30

4. Results

The results obtained for each case are presented below. The analysis includes stress distributions, contact forces, displacements, and particle breakage.

Cyclic loading was applied to the central sleeper. Numerical models with this level of detail, simulating tens of thousands of load cycles is computationally demanding. Therefore, results corresponding to 300 load cycles applied at a frequency of 10 Hz, associated with a train speed of 85 km/h, are presented only. The focus is placed on the deformation trend and the rate of deformation accumulation. After 300 cycles, the deformation rate $\Delta\delta/\Delta N$ became very small, and the accumulated deformation remained below 0.004 mm/s. Based on these observations, the system is considered to operate within the shakedown stage under the analyzed conditions. For very long-term behaviour, the present model may be complemented with simplified approaches or extrapolation schemes; however, the operative stage is already identified.

4.1. Factor of Safety Considerations

To examine stress transmission through the different layers of the track support system, Figure 14 presents the stress profiles with depth along the transverse section. Interestingly high deviatoric stress values, defined as σ_d are observed at the sleeper–ballast interface, which progressively dissipate through the ballast layer. The marked increase in deviatoric stress across all analyzed points highlights its role as the primary factor governing the accumulated permanent strain of the ballast under repeated loading.

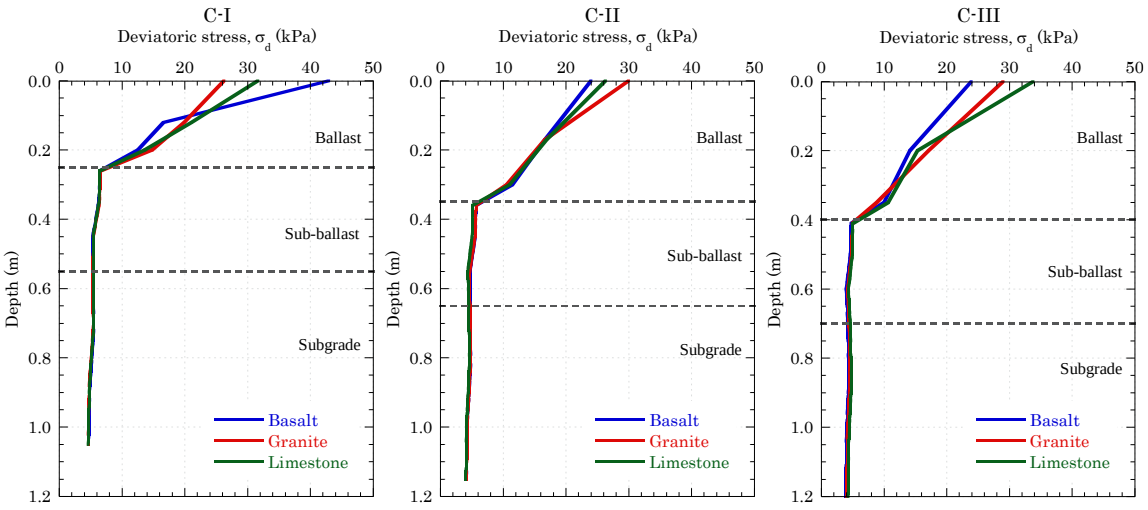

Figure 14. Deviatoric stress profile with depth along the transverse section.

4.2. Characterization of Plastic Deformation

Under repetitive loading, the mechanical behavior of granular materials is characterized by the development of permanent axial deformations. In the initial stages of cyclic loading, these deformations increase rapidly due to the internal reorganization of particles, a phenomenon

 doi:10.20944/preprints202602.2004.v1

commonly called "cyclic densification". After this initial phase, the material's response is governed by the shakedown regime, which can be classified into three domains: plastic shakedown, where the material reaches a stable state with negligible deformation increments per cycle; plastic creep, in which deformations continue to accumulate progressively but at a reduced rate; and plastic collapse/ratcheting, characterized by unsteady accumulation of deformations leading to rapid failure (Figure 15). The transition between these regimes is strongly influenced by the confining pressure and the magnitude and frequency of the applied load. It is observed that increases in deviatoric stress and frequency tend to increase permanent deformations and shift the material response toward more unstable states [32,33].

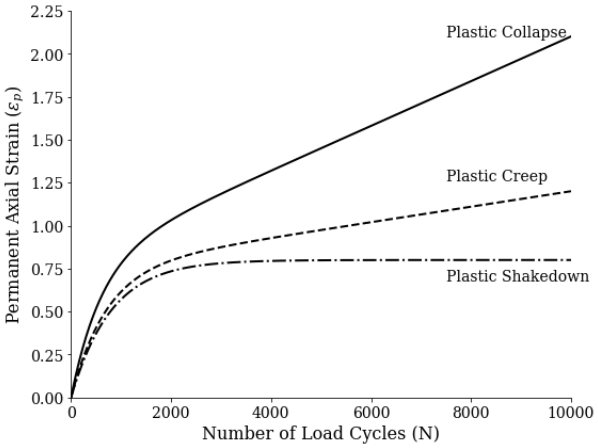

Figure 15. Responses of granular materials under cyclic loading.

Figure 16 shows the deformation histories as a function of the number of load cycles at the control point located beneath the central sleeper (as indicated in Figure 12). Permanent strain of the particle assembly increases significantly during the first approximately 250 load cycles. Beyond this stage, the accumulation of permanent strain stabilizes at an approximately constant rate, which is consistent with a shakedown-type response.

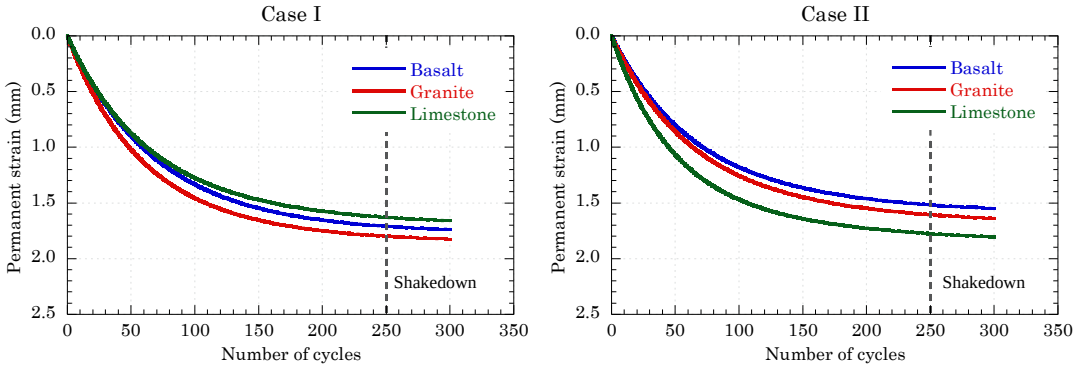

 doi:10.20944/preprints202602.2004.v1

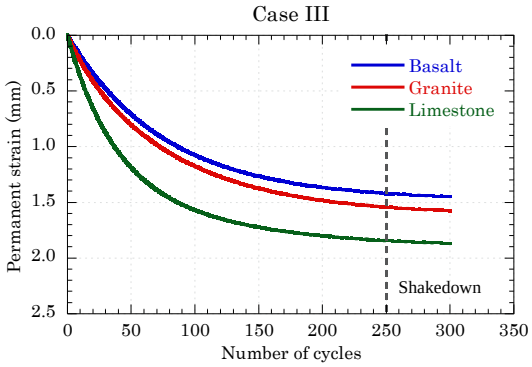

Figure 16. Displacement histories during cyclic loading.

Figure 17 presents the vibration velocities of ballast particles at the end of 300 load cycles. A clear reduction in particle velocity is observed with increasing ballast height, together with a downward shift of the central sleeper. In addition, higher particle velocities are consistently observed for limestone ballast across all analyzed cases.

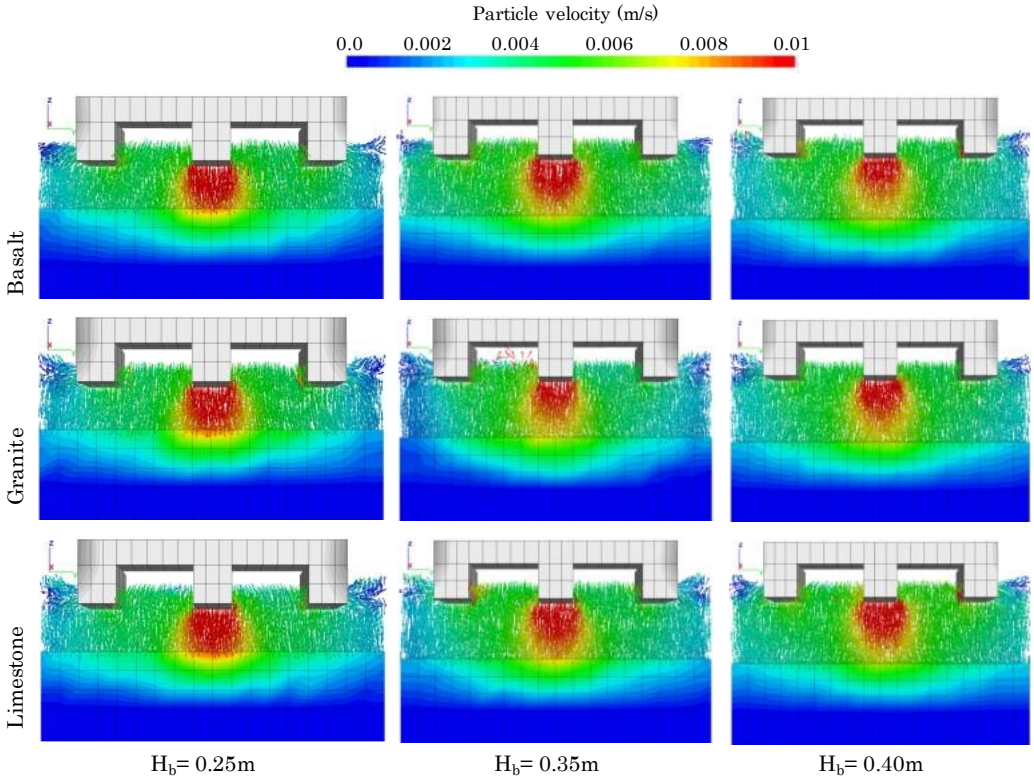

Figure 17. Particle velocities at the end of 300 load cycles.

4.3. Particle Breakage

Figure 18 illustrates the spatial distribution of particle breakage for all analyzed cases. The highest levels of particle fragmentation are concentrated at the sleeper–ballast interface, where increased deviatoric stresses lead to higher transmission of shear forces, leading to elevated breakage indices.

 doi:10.20944/preprints202602.2004.v1

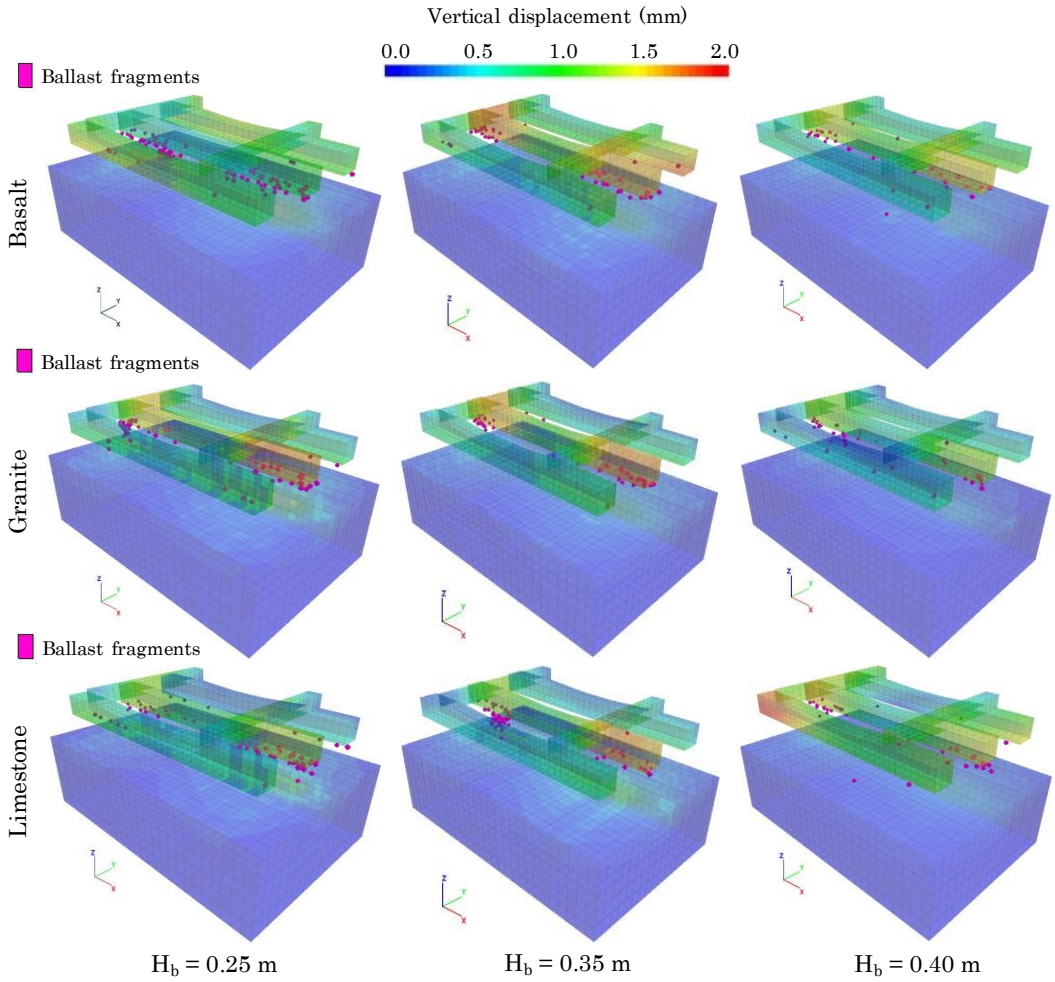

Figure 18. Fragmented particles after 300 load cycles.

With respect to particle breakage, a progressive reduction in the number of fragments is observed as ballast height increases. The Marsal breakage index (Bg) [34] exhibits clear reductions with increasing height. The Indraratna breakage index (BBI) [35] follows a similar trend, although with some differences in relative magnitude. At a ballast height of 0.25 m, basalt exhibits the highest BBI value (0.357), while granite and limestone show nearly identical values (0.324 and 0.323, respectively). At 0.35 m, limestone presents the highest BBI (0.322), followed by basalt (0.294) and granite (0.253). At a height of 0.40 m, the ranking changes, and the overall values decrease to 0.214 (limestone), 0.170 (granite), and 0.156 (basalt), as shown in Figures 19 and 20.

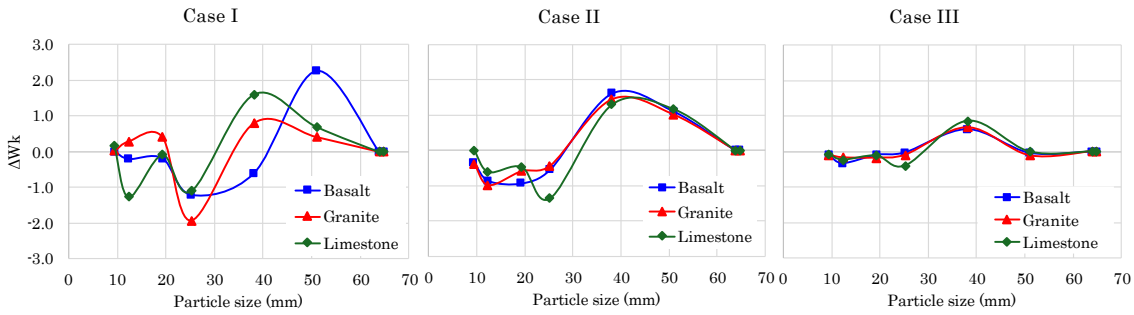

Figure 19. Particle breakage index, Bg.

 doi:10.20944/preprints202602.2004.v1

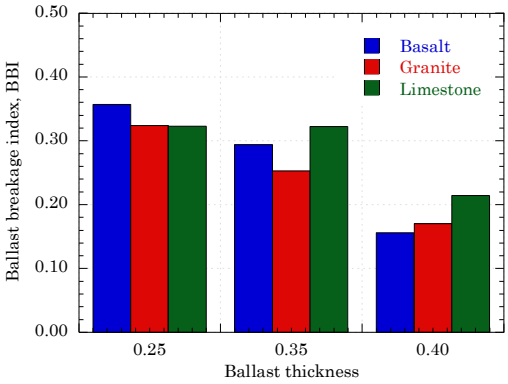

Figure 20. Ballast particle breakage index, BBI.

Figure 21 shows the evolution of the particle size distribution (PSD) of basalt under cyclic loading for a ballast thickness of 35 cm (Case II). An increase in the proportion of smaller fragments is observed, particularly within the 20–40 mm size range, while the grading curves preserve their overall shape. This shift of the distribution toward smaller particle sizes is a direct consequence of the progressive fragmentation of larger particles, which supply finer size fractions of material.

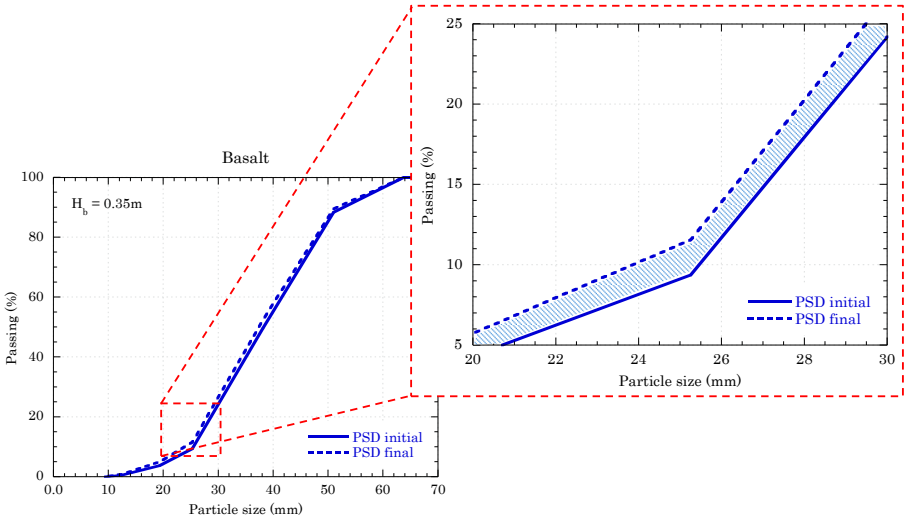

Figure 21. Change in PSD for Case II with basalt.

4.4. Factor of Safety Sub-Ballast

The factor of safety (FS) at the sub-ballast layer increases with increasing ballast thickness, as depicted in Figure 22. The factor of safety was computed with the expression (8). This trend is directly related to the progressive reduction of stresses and displacements. For a thickness of 0.25 m, the FS values are less than 2.0 (a reference established by AREMA [11]), while for 0.35 m, a slightly higher value is obtained. The 0.40 m thickness provides the highest factor of safety for the three materials, with an FS of 2.40 for granite.

$$FS = \frac{F_R}{F_A} = \frac{\tau_{res}}{\tau_{oct}} \tag{8}$$

$$\tau_{oct} = \frac{\sqrt{(\sigma_1 - \sigma_2)^2 + (\sigma_2 - \sigma_3)^2 + (\sigma_3 - \sigma_1)^2}}{3} \tag{9}$$

$$p' = \frac{\sigma_1 + \sigma_2 + \sigma_3}{3} \tag{10}$$

 doi:10.20944/preprints202602.2004.v1

$$\tau_{res} = c + p' \tan \phi \quad (11)$$

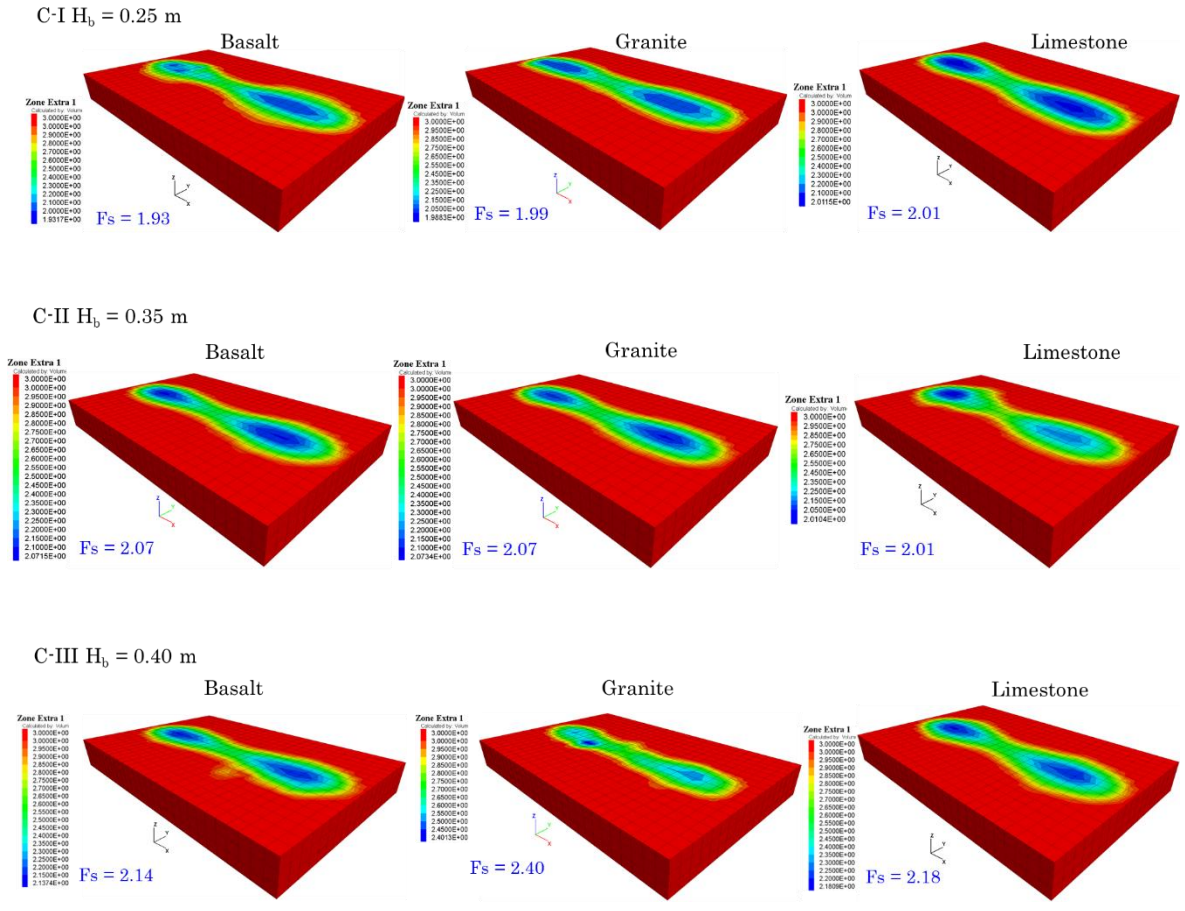

Figure 22. FS sub ballast.

5. Ballast Performance Assessment

This section introduces a novel approach that relates the conventional factor of safety obtained for rail track support to the expected permanent strain. Beginning with the continuous models, the ballast safety factor was calculated using expression (8) for the corresponding material. However, because continuous models cannot adequately represent the accumulation of permanent deformations in granular materials, these safety factors were compared with the permanent strains obtained from hybrid DEM–FDM models for the same digital twin.

First, the influence of ballast layer thickness on each material type was analyzed and compared with the safety factor calculated using conventional continuous models. The results, shown in Figure 23, demonstrate similar behavior across all materials: the safety factor increases with ballast thickness. However, the FS values for limestone ballast are consistently lower, primarily due to its less competent mechanical properties compared with basalt and granite.

 doi:10.20944/preprints202602.2004.v1

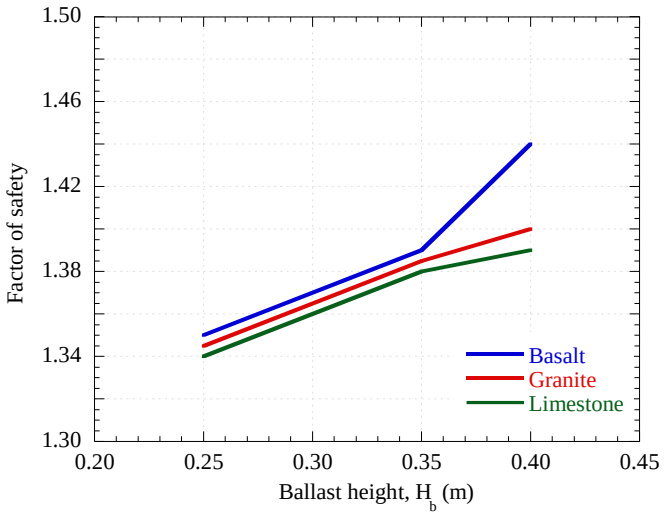

Figure 23. Factor of safety for ballast with a continuous model.

Subsequently, the combined influence of layer thickness and material type on the permanent deformations obtained from the hybrid models was evaluated, as shown in Figure 24. A similar trend is observed between basalt and granite, which reduces deformation as thickness increases. In contrast, the behavior of limestone ballast differs significantly: increasing thickness leads to greater permanent deformation, an effect associated with increased particle breakage and granular degradation, as also reported by other research [36–38].

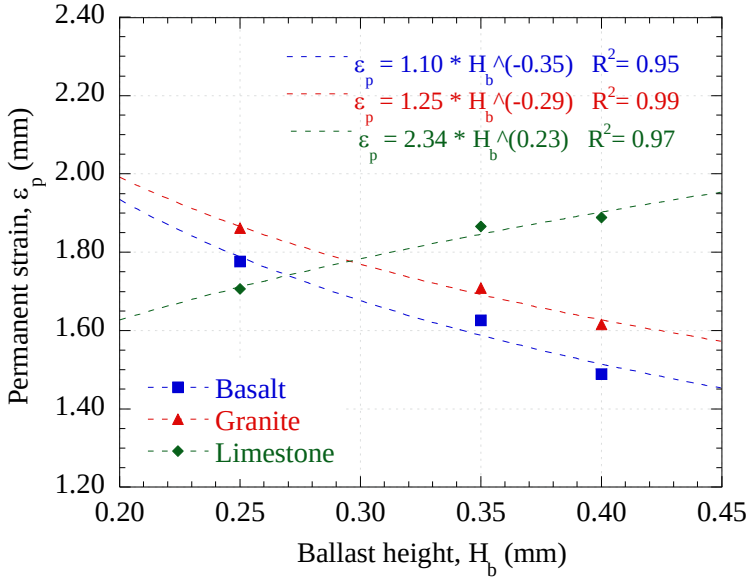

Figure 24. Permanent ballast strain for various heights.

Finally, a direct comparison was made between accumulated permanent strain and the safety factor to establish a quantitative relationship between the two, as shown in Figure 25.

 doi:10.20944/preprints202602.2004.v1

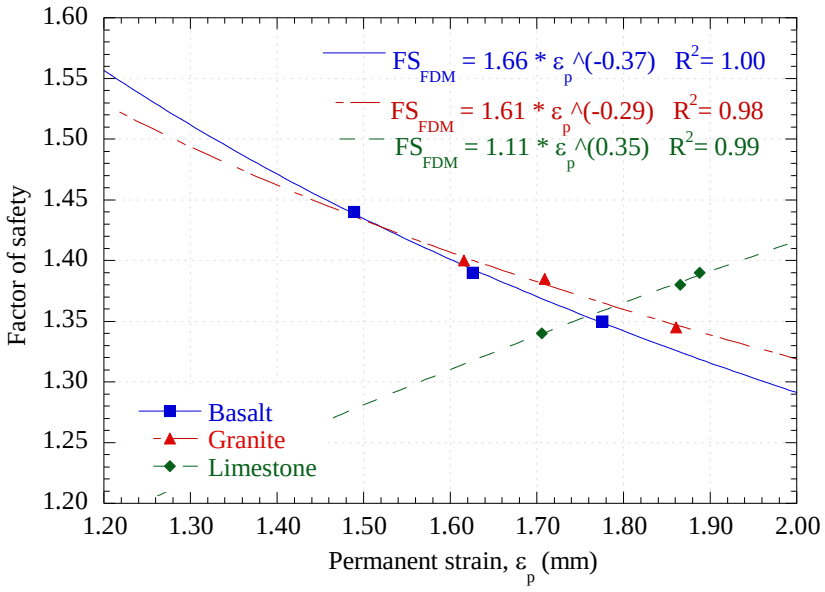

Figure 25. Relationship between ballast permanent strain and factor of safety.

The numerical models enabled the development of empirical correlations between key performance variables: the safety factor obtained from the continuous model (FS_{FDM}) and permanent strain (ε_p). The fitted curves, expressed as $FS_{FDM} = a{\varepsilon_p}^b$, where a and b are parameters that depend on the type of material, provided the following parameters for each material:

$$FS_{FDM} = 1.66{\varepsilon_p}^{-0.37} \quad \text{(Basalt)} \quad (12)$$

$$FS_{FDM} = 1.61{\varepsilon_p}^{-0.29} \quad \text{(Granite)} \quad (13)$$

$$FS_{FDM} = 1.11{\varepsilon_p}^{0.35} \quad \text{(Limestone)} \quad (14)$$

The equations for basalt and granite indicate that an increase in permanent deformation is associated with a reduction in the safety factor. This behavior is typical of granular materials that, after deforming plastically, exhibit a progressive loss of shear strength until reaching a residual strength.

The limestone equation shows an opposite trend: the FS increases with deformation. This confirms a change in the dominant mechanism, associated with particle degradation and breakage, as well as with the reorganization and compaction of angular limestone particles under cyclic loading. Thus, in this case, the failure occurs through excessive deformation, independently of the factor of safety.

Different modeling approaches influence the observed performance: the factor of safety (FS), obtained from finite-difference models (FDM), reflects an increase in apparent strength due to macroscopic densification but does not capture the internal mechanisms of granular degradation. Conversely, hybrid DEM–FDM simulations that explicitly represent the granular nature of ballast show that particle fragmentation and reordering lead to irreversible, cumulative deformation. Thus, the apparent contradiction between a rising FS and larger deformations is not an inconsistency but rather the result of different physical mechanisms in each model, highlighting the need for performance-based assessment approaches that explicitly incorporate granular damage and deformation accumulation.

The safety factors (FS) of the hybrid models were determined using the same formulation described in Equations (8–11). Since discrete media do not explicitly define macroscopic cohesion (c) or friction angle (ϕ), cohesion was assumed to be zero, and the macroscopic friction angle was obtained from numerical triaxial tests performed on the calibrated DEM specimen. The stress tensor was computed for each measurement sphere, enabling evaluation of the local stress state. Figure 26

 doi:10.20944/preprints202602.2004.v1

presents the FS obtained with the hybrid model as a function of permanent strain, while Figure 27 shows all the FS for the different thicknesses evaluated.

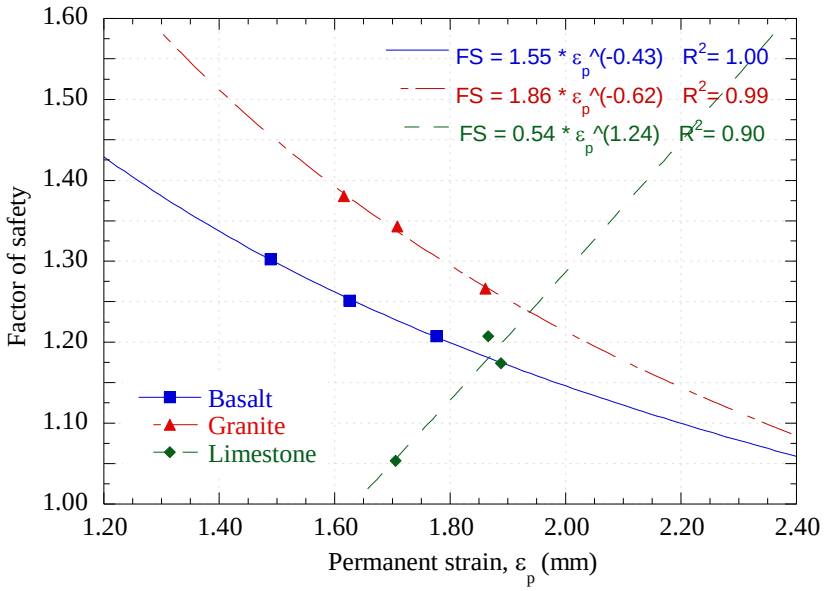

Figure 26. Relationship between ballast permanent strain and factor of safety obtained with the hybrid models.

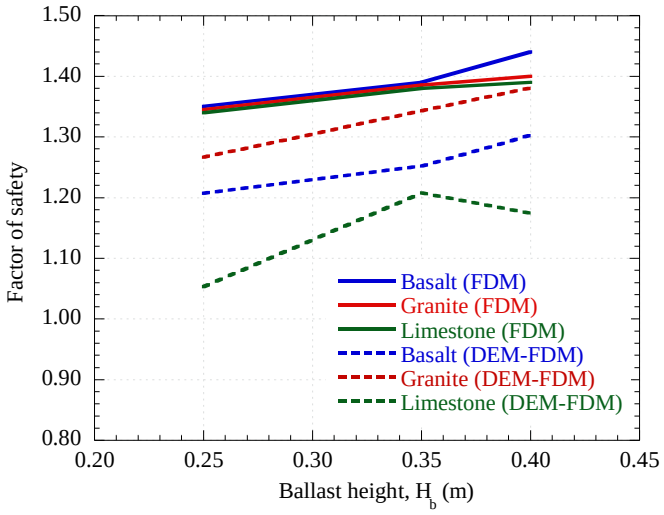

Figure 27. Comparison of the safety factors calculated with all models considered.

A systematic difference is observed between the modeling approaches: the hybrid DEM–FDM model consistently predicts lower FS values than the continuous FDM model, indicating that the latter tends to overestimate stability. The magnitude of the discrepancy depends on the material; limestone shows the greatest differences (up to approximately 22%), basalt exhibits intermediate values (8–10%), and granite displays nearly convergent results at higher ballast heights.

These differences are associated with micromechanical behavior. The hybrid model captures local stress redistributions and progressive failure mechanisms, while the continuous model smooths the stress fields and assumes homogeneity, which can hide local instabilities. Consequently, the hybrid approach provides more conservative estimates, particularly near critical conditions (FS ≈ 1.0–1.2), highlighting the importance of incorporating micromechanical effects in marginal stability analysis.

 doi:10.20944/preprints202602.2004.v1

Given that continuum FDM/FEM models remain the standard tool in engineering practice due to their computational efficiency, the results of this study support the introduction of a material-dependent correction factor to account for microstructural degradation effects captured by DEM simulations.

The corrected safety factor may be estimated as:

$$FS_{corr} = \eta \cdot FS_{FDM} \quad (15)$$

where η represents a micromechanical reduction factor calibrated against DEM–FDM simulations, associated to plastic deformation mainly due to particle rupture, particle rotation, and force transmission (i.e., all the micromechanical interactions).

Table 7 presents the safety and influence factors obtained from degradation. For the analyzed range (ballast height 0.25–0.40 m and permanent strains 1.5–1.9 mm), the following values are recommended: $\eta = 0.90, 0.97, 0.84$ for basalt, granite, and limestone.

Table 7. Factors of safety and micromechanical influence factors.

Material	Height, H_b (m)	Permanent strain, ε_p (mm)	Factor of safety		Micromechanical influence factor, η	Average micromechanical influence factor, η_{avg}
			FDM	DEM-FDM		
Basalt	0.25	1.78	1.35	1.21	0.89	0.90
	0.35	1.63	1.39	1.25	0.90	
	0.40	1.49	1.44	1.30	0.90	
Granite	0.25	1.86	1.35	1.27	0.94	0.97
	0.35	1.71	1.39	1.34	0.97	
	0.40	1.62	1.40	1.38	0.99	
Limestone	0.25	1.71	1.34	1.05	0.79	0.84
	0.35	1.87	1.38	1.21	0.88	
	0.40	1.89	1.39	1.17	0.84	

These values provide a conservative yet practical adjustment for force chain and particle breakage mechanisms not represented in continuum formulations. The correction preserves the efficiency of conventional numerical approaches while improving the reliability of stability predictions for crushable granular materials.

The proposed correction factors are valid within the investigated geometric and loading conditions and should be recalibrated if material grading, loading regime, or confinement conditions differ significantly.

Having established the micromechanical correction and the strain–safety relationship, a performance-based design criterion can be formulated.

5.1. Deformation-Based Performance Criterion

While the micromechanical correction factor improves the predictive capability of conventional safety factors, stability alone does not guarantee acceptable long-term performance in granular materials subjected to cyclic loading. Therefore, a performance-based threshold was introduced by defining an optimal safety factor, FS_{opt}, associated with the onset of plastic shakedown.

The empirical relationship obtained from the numerical simulations is expressed as:

$$FS_{FDM} = a{\varepsilon_p}^b \quad (16)$$

and incorporating the micromechanical correction factor:

$$FS_{corr} = \eta FS_{FDM} \quad (17)$$

 doi:10.20944/preprints202602.2004.v1

The optimal safety factor FS_{opt} was defined as the onset of plastic shakedown, corresponding to the condition in which the incremental rate of permanent strain accumulation with respect to the number of load cycles becomes negligible, i.e., $(d\varepsilon_p/dFS) \to 0$.

Rather than being assumed a priori, FS_{opt} was obtained directly from the permanent deformation evolution curves derived from the hybrid DEM–FDM simulations. Specifically, the onset of plastic shakedown was identified in Figure 16 as the deformation state at which the permanent strain–cycle curve approaches a horizontal asymptote, indicating stabilization of strain accumulation under cyclic loading.

The safety factor corresponding to this stabilized deformation state was subsequently extracted from the DEM–FDM simulations. Therefore, FS_{opt} is numerically derived and physically linked to the micromechanical stabilization of particle rearrangement and degradation processes. The resulting material-specific values were 1.30 for basalt, 1.35 for granite, and 1.20 for limestone.

The performance-based design criterion was therefore established as:

$$FS_{corr} \geq FS_{opt} \tag{18}$$

Substituting Equation (17) into Equation (18) and replacing FS_{FDM} using Equation (16) allows the requirement to be expressed directly in terms of permanent strain:

$$\varepsilon_p \leq \left(\frac{FS_{opt}}{\eta a}\right)^{1/b} \tag{19}$$

Therefore, the traditional stability-based verification is reformulated into a deformation-controlled performance requirement directly linked to long-term serviceability. The design requirement is therefore reformulated directly in terms of allowable permanent strain.

$$\varepsilon_p \leq \varepsilon_{p,adm} \tag{20}$$

The allowable permanent strain is thus given by:

$$\varepsilon_{p,adm} = \left(\frac{FS_{opt}}{\eta a}\right)^{1/b} \tag{21}$$

Substituting the calibrated material parameters and the corresponding FS_{opt} values into Equation (21) yields admissible permanent strains of 1.47 mm for basalt, 1.66 mm for granite, and 2.05 mm for limestone. These values represent the maximum allowable permanent deformation compatible with shakedown-based performance under the investigated loading conditions.

Finally, the relationship between permanent strain and ballast thickness was expressed as:

$$\varepsilon_p = kH_b^m \tag{22}$$

Combining Equations (21) and (22), the minimum required ballast thickness to satisfy the shakedown-based criterion is:

$$H_{b,min} = \left(\frac{\varepsilon_{p,adm}}{k}\right)^{1/m} \tag{23}$$

Using the proposed methodology, deformation-controlled ballast design charts were derived, as shown in Figures 28 and 29.

Figure 28(a) presents the corrected safety factor FS_{corr} as a function of permanent strain, including the target stability thresholds FS_{opt} determined for each evaluated material. These curves define the admissible deformation domain associated with the onset of plastic shakedown and provide a direct graphical verification of the performance-based criterion.

Figure 29 illustrates the relationship between permanent strain and ballast layer thickness. From this relationship, the minimum required ballast thickness can be determined to ensure compliance with the admissible permanent strain limits linked to the corresponding FS_{opt}. Consequently, the design requirement is reformulated from a purely stability-based check into a deformation-controlled thickness selection procedure.

Preprints.org (www.preprints.org) | NOT PEER-REVIEWED | Posted: 2 March 2026 doi:10.20944/preprints202602.2004.v1

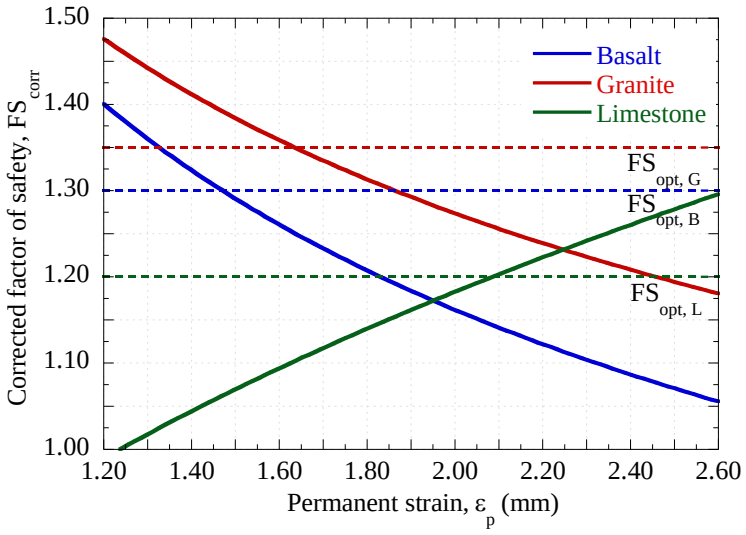

Figure 28. Corrected safety factor versus permanent strain, including the target stability threshold.

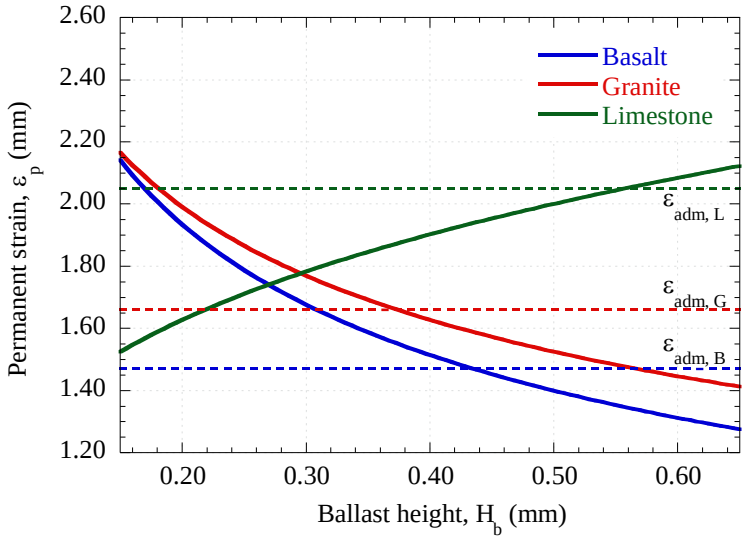

Figure 29. Permanent strain versus ballast thickness, showing allowable deformation limits and the minimum required thickness.

Therefore, the curves shown in Figure 28 can be analytically reproduced using the following material-specific expressions for the corrected safety factor:

$$FS_{corr,basalt} = 1.50\varepsilon_p{}^{-0.37} \quad (24)$$

$$FS_{corr,granite} = 1.56\varepsilon_p{}^{-0.29} \quad (25)$$

$$FS_{corr,limestone} = 0.93\varepsilon_p{}^{0.35} \quad (26)$$

Similarly, the relationships shown in Figure 29 are described by the following permanent strain–thickness correlations:

$$\varepsilon_{p,basalt} = 1.10H_b{}^{-0.35} \quad (27)$$

$$\varepsilon_{p,granite} = 1.25H_b{}^{-0.29} \quad (28)$$

 doi:10.20944/preprints202602.2004.v1

$$\varepsilon_{p,limestone} = 2.34{H_b}^{0.23} \quad (29)$$

Table 8 summarizes the application of the proposed deformation-controlled methodology to the evaluated configurations. Only granite with a ballast thickness of 0.40 m satisfies stability, deformation, and minimum thickness criteria simultaneously. Basalt exhibits marginal stability at 0.40 m but does not meet the minimum thickness requirement. Limestone requires a significantly greater thickness (0.56 m) to ensure operation within the shakedown regime.

Table 8. Verification of the proposed deformation-based criteria for different ballast materials.

Material	Height, H_b (m)	Permanent strain, ε_p (mm)	FS_{FDM}	FS_{corr}	FS_{opt}	ε_{adm} (mm)	H_{min} (m)
Basalt	0.25	1.78	1.35	1.21	1.30	1.47	0.43
	0.35	1.63	1.39	1.25	1.30	1.47	
	0.40	1.49	1.44	1.30	1.30	1.47	
Granite	0.25	1.86	1.35	1.27	1.35	1.66	0.38
	0.35	1.71	1.39	1.34	1.35	1.66	
	0.40	1.62	1.40	1.38	1.35	1.66	
Limestone	0.25	1.71	1.34	1.05	1.20	2.05	0.56
	0.35	1.87	1.38	1.21	1.20	2.05	
	0.40	1.89	1.39	1.17	1.20	2.05	

The final design and verification procedure integrates numerical simulation results, micromechanical correction, and deformation-based performance limits into a unified framework.

The complete procedure can be summarized as follows:

1. Numerical stability assessment

   Obtain the safety factor from FDM simulations:

$$FS_{FDM}$$

2. Micromechanical correction

   Incorporate particle-scale effects through:

$$FS_{corr} = \eta FS_{FDM}$$

where η is the material-dependent correction coefficient.

3. Determination of admissible permanent strain

   From the strain–safety correlation:

$$\varepsilon_{p,adm} = \left(\frac{FS_{opt}}{\eta a}\right)^{\frac{1}{b}}$$

where a and b are regression parameters material dependent.

4. Minimum required ballast thickness

   Using the strain–thickness relationship:

$$H_{min} = \left(\frac{\varepsilon_{p,adm}}{k}\right)^{1/m}$$

   Final Verification Criteria

   A ballast layer satisfies the shakedown-controlled condition when:

$$FS_{corr} \geq FS_{opt}$$
$$\varepsilon_p \leq \varepsilon_{p,adm}$$
$$H_b \geq H_{min}$$

 doi:10.20944/preprints202602.2004.v1

These three conditions define a deformation-controlled stability domain, ensuring simultaneously the compliance with the stability safety factor.

6. Discussion

The applicability of the proposed correlations is subject to the conditions and assumptions under which they were derived. Thus, the prosed equations are valid for the specific parameter range of the model: ballast heights between 0.25 and 0.40 m, the type of applied load, and the range of studied permanent strains (approximately 1.5 to 1.9 mm). Critical factors such as moisture, fine contamination, degradation due to abrasion under cyclic loads, and the presence of sub-ballast or sub-grade of different qualities are not explicitly incorporated into the correlations. The adjusted potential relationship may not hold its shape outside the analyzed range, especially for limestone, whose positive exponent (b = +0.29) likely represents only the initial phase of compaction. It is expected that, at greater deformations, a peak in strength will be reached, followed by a degradation phase, a pattern not captured by the current data

5. Conclusions

This study presents a numerical investigation to assess the performance of the track support system. A parallel modeling strategy was adopted, combining a hybrid DEM–FDM approach with a conventional continuum model based on the finite difference method to establish a quantitative relationship between the safety factor (FS) and the accumulated permanent strain (ε_p).

The results demonstrate that ballast height and material type strongly influence accumulated permanent strain, stress transmission, and particle breakage. For the loading and speed conditions analyzed, most configurations operate within a stable shakedown regime.

The stress distribution showed that the highest deviatoric stresses are concentrated at the sleeper-ballast interface and gradually decrease with depth. This concentration of stresses explains the higher fracture rates observed in that area. It was confirmed that increasing the thickness of the ballast layer significantly reduces granular degradation, with up to 50% reduction in BBI when increasing the ballast layer height from 0.25 to 0.40 meters. Among the materials, basalt exhibited the greatest resistance to fracture at reduced thicknesses, while limestone showed greater degradation at larger thicknesses, associated with its lower mechanical competence and higher susceptibility to breakage. The safety factor calculated in the sub-ballast layer showed a clear dependence on ballast thickness for values of 0.35 m and 0.40 m.

A novel approach was developed that relates the FS obtained through continuous models with the accumulated permanent strain captured by hybrid simulations, establishing material-specific empirical correlations of the form $FS_{FDM} = a{\varepsilon_p}^b$. For basalt and granite ballast, an inverse relationship was observed between safety factor and accumulated permanent deformation, indicating that greater stability is associated with improved deformation performance. In contrast, limestone showed a different trend, suggesting that higher stability margins do not necessarily imply reduced permanent deformation, likely because it is more susceptible to particle breakage.

The comparison between continuum and hybrid simulations revealed a systematic overestimation of stability by conventional FDM models. This difference was quantified using a material-dependent micromechanical influence factor, η, defined as the ratio of the hybrid to the continuum safety factor. Within the investigated range, recommended correction values are $\eta = 0.90$ for basalt, $\eta = 0.97$ for granite, and $\eta = 0.84$ for limestone. The incorporation of this factor allows the adjustment of conventional continuum-based safety factors such as $FS_{corr} = \eta \cdot FS_{FDM}$.

This correction provides a practical means to implicitly account for degradation and particle breakage mechanisms without requiring detailed DEM simulations in engineering practice. The proposed influence factor, therefore, bridges advanced micromechanical modeling and standard design procedures, improving the reliability of stability assessments in railway systems.

 doi:10.20944/preprints202602.2004.v1

However, stability alone does not guarantee satisfactory long-term performance under cyclic loading. To address this limitation, a deformation-based performance criterion was introduced by defining an optimal safety factor, FS_{opt}, associated with the onset of plastic shakedown. This threshold was identified as the point where the incremental rate of permanent strain accumulation becomes negligible. The resulting values were 1.30 for basalt, 1.35 for granite, and 1.20 for limestone.

By combining the empirical stability–deformation relationship with the micromechanical correction factor, the design requirement can be reformulated directly in terms of allowable permanent strain. This leads to a material-dependent admissible strain limit, $\varepsilon_{p,adm}$, from which the minimum required ballast thickness can be derived through the established strain–thickness relationship. Consequently, the minimum ballast height ensuring shakedown-controlled performance can be determined analytically.

This framework enhances the traditional safety-factor-based design approach into an integrated stability–deformation design methodology. Rather than prescribing thickness solely from stress-based criteria, the proposed approach enables the explicit control of long-term permanent deformation while implicitly accounting for micromechanical degradation mechanisms.

Although the correlations and correction factors are limited to the modeled geometric and loading conditions and do not explicitly account for fouling, moisture, long-term abrasion, or subgrade variability, the results demonstrate the potential of hybrid numerical modeling to support more rational, material-sensitive, and performance-oriented railway design and maintenance strategies. Future research will extend this framework to incorporate subgrade response, long-term cyclic degradation mechanisms, and field-calibrated dynamic loading scenarios, enabling a more comprehensive evaluation of track performance under evolving operational demands.

Author Contributions: Conceptualization, J.M.M. and N.O.; methodology, J.M.M. and N.O.; software, N.O.; validation, J.M.M. and N.O.; formal analysis, N.O.; investigation, J.M.M. and N.O.; resources, J.M.M.; data curation, N.O.; writing—original draft preparation, N.O.; writing—review and editing, J.M.M. and N.O.; visualization, N.O. All authors have read and agreed to the published version of the manuscript.

Funding: This research received no external funding.

Institutional Review Board Statement: Not applicable.

Informed Consent Statement: Not applicable.

Data Availability Statement: The original contributions presented in this study are included in the article. Further inquiries can be directed to the corresponding author.

Conflicts of Interest: The authors declare no conflicts of interest.

Abbreviations

The following abbreviations are used in this manuscript:

AREMA	**American Railway Engineering and Maintenance-of-Way Association**
BBI	**Ballast Breakage Index**
Bg	**Breakage index Marsal**
DEM	**Discrete element method**
FDM	**Finite difference method**

References

1. Indraratna, B.; Nimbalkar, S.; Christie, D. Ballast degradation and permanent deformation under cyclic loading. J. Geotech. Geoenviron. Eng. **2011**, 137, 557–567.
2. Kaewunruen, S.; Remennikov, A.M. Dynamic behavior of railway ballast. Eng. Fail. Anal. **2009**, 16, 1520–1532.

 doi:10.20944/preprints202602.2004.v1

3. Sayeed, M.A.; Shahin, M.A. Design of ballasted railway track foundations using numerical modelling. Part I: Development. Can. Geotech. J. **2018**, 55, 353–368.
4. Powrie, W.; Le Pen, L.; Clayton, C. Behaviour of railway track granular layers. Proc. ICE Ground Improv. **2016**, 169, 243–259.
5. Huang, H.; Tutumluer, E.; Hashash, Y.M.A. Effects of ballast gradation on performance. Railw. Eng. Sci. **2016**, 24, 213–223.
6. Shi, C.; Fan, Z.; Connolly, D.P.; Jing, G.; Markine, V.; Guo, Y. Railway ballast performance: Recent advances in the understanding of geometry, distribution and degradation. Transp. Geotech. **2023**, 41, 101042.
7. Lackenby, J.; Indraratna, B.; Christie, D.; Brown, R. Effect of confining pressure on ballast deformation. J. Geotech. Geoenviron. Eng. **2007**, 133, 1467–1470.
8. Li, L.; Liu, W.; Ma, M.; Jing, G.; Liu, W. Research on the dynamic behaviour of the railway ballast assembly subject to low loading condition based on a tridimensional DEM–FDM coupled approach. Constr. Build. Mater. **2019**, 218, 135–149.
9. Bian, X.; Huang, H.; Li, T.; Liu, P. Numerical modeling of ballasted railway track dynamics using discrete–continuous approaches. Transp. Geotech. **2020**, 23, 100322.
10. Li, T.; Gao, Y.; Zhong, Y.; Xu, P.; Yang, G. Coupled DEM–FDM study on the dynamic performance of ballast–subgrade system under cyclic axle loading. Transp. Geotech. **2025**, 101737.
11. AREMA. Manual for Railway Engineering; American Railway Engineering and Maintenance-of-Way Association: Lanham, MD, USA, **2013**; Volume 2, pp. 55–57.
12. European Committee for Standardization. EN 13803:2018 Railway Applications—Track—Track Alignment Design Parameters—Track Gauges 1435 mm and Wider; CEN: Brussels, Belgium, **2018**.
13. Heath, D.L.; Shenton, M.J.; Sparrow, R.W.; Waters, J.M. Design of conventional rail track foundations. Proc. Inst. Civ. Eng. **1972**, 51, 251–267.
14. UIC. UIC Code 719 R: Earthworks and Track-Bed Layers for Railway Lines; International Union of Railways: Paris, France, **2008**.
15. West Japan Railway Company. Construction and Maintenance Standards for Shinkansen Track; West Japan Railway Company: Osaka, Japan, **2002**.
16. Network Rail. Formation Treatments RT/CE/C/039; Network Rail: London, UK, 2003.
17. Li, D.; Selig, E.T. Method for railroad track foundation design. I: Development. J. Geotech. Geoenviron. Eng. 1998, 124, 316–322.
18. Itasca Consulting Group, Inc. PFC3D—Particle Flow Code in 3 Dimensions, Theory and Background; Itasca Consulting Group, Inc.: Minneapolis, MN, USA, **2019**.
19. Iwashita, K.; Oda, M. Rolling resistance at contacts in simulation of shear band development by DEM. J. Eng. Mech. **1998**, 124, 285–292.
20. Ai, J.; Chen, J.F.; Rotter, J.M.; Ooi, J.Y. Assessment of rolling resistance models in discrete element simulations. Powder Technol. **2011**, 206, 269–282.
21. Ciantia, M.O.; Arroyo, M.; Calvetti, F.; Gens, A. An approach to enhance efficiency of DEM modelling of soils with crushable grains. Géotechnique 2015, 65, 91–110.
22. Russell, A.R.; Muir Wood, D. Point load tests and strength measurements for brittle spheres. Int. J. Rock Mech. Min. Sci. **2009**, 46, 272–280.
23. McDowell, G.R.; de Bono, J.P. On the micromechanics of one-dimensional normal compression. Géotechnique **2013**, 63, 895–908.
24. Einav, I. Breakage mechanics—Part I: Theory. J. Mech. Phys. Solids **2007**, 55, 1274–1297.
25. Indraratna, B.; Ionescu, D.; Christie, H.D. Shear behavior of railway ballast based on large-scale triaxial tests. J. Geotech. Geoenviron. Eng. **1998**, 124, 439–449.
26. Xiao, J.; Zhang, D.; Wei, K.; Luo, Z. Shakedown behaviors of railway ballast under cyclic loading. Constr. Build. Mater. **2017**, 155, 1206–1214.
27. Qian, Y.; Tutumluer, E.; Hashash, Y.M.; Ghaboussi, J. Triaxial testing of new and degraded ballast under dry and wet conditions. Transp. Geotech. **2022**, 34, 100744.
28. ASTM International. ASTM C136/C136M-19: Standard Test Method for Sieve Analysis of Fine and Coarse Aggregates; ASTM International: West Conshohocken, PA, USA, **2019**.

 doi:10.20944/preprints202602.2004.v1

29. Tran, V.D.; Meguid, M.A.; Chouinard, L.E. Discrete element and experimental investigations of the earth pressure distribution on cylindrical shafts. Int. J. Geomech. **2014**, 14, 80–91.
30. Xiao, Y.; Shen, Z.; Tan, P.; Hua, W.; Wang, M.; Jitsangiam, P. Evaluating enhancement effect of bottom groove shape on lateral resistance of frictional sleepers in ballasted railway track via hybrid DEM–FDM approach. Constr. Build. Mater. **2024**, 436, 136755.
31. Mayoral, J.M.; Olivera, N. Performance Evaluation of Conventional and Recycled Ballast Materials: A Coupled FDM-DEM Approach Considering Particle Breakage. *Appl. Sci.* **2025**, *15*, 11460.
32. Werkmeister, S.; Dawson, A.R.; Wellner, F. Permanent deformation behavior of granular materials and the shakedown concept. Transp. Res. Rec. **2001**, 1757, 75–81.
33. Malisetty, R.S.; Indraratna, B.; Qi, Y.; Rujikiatkamjorn, C. Estimating the shakedown limit for granular materials under cyclic loading. In Proceedings of the International Conference on Transportation Geotechnics, Singapore, 20–22 November **2024**; pp. 183–191.
34. Marsal, R.J. Large scale testing of rockfill materials. J. Soil Mech. Found. Div. 1967, 93, 27–43.
35. Indraratna, B.; Lackenby, J.; Christie, D. Effect of confining pressure on the degradation of ballast under cyclic loading. Géotechnique **2005**, 55, 325–328.
36. Bian, X.; Shi, K.; Li, W.; Luo, X.; Tutumluer, E.; Chen, Y. Quantification of railway ballast degradation by abrasion testing and computer-aided morphology analysis. J. Mater. Civ. Eng. **2021**, 33, 04020411.
37. Indraratna, B.; Ngo, T.; Rujikiatkamjorn, C. Performance of ballast influenced by deformation and degradation: Laboratory testing and numerical modeling. Int. J. Geomech. **2020**, 20, 04019138.
38. Andrade, G.; Dieguez, C.; Lima, B.; Guimarães, A. Evaluation of limestone aggregates for railway ballast: Particle characteristics and shear strength analysis. Soils Rocks 2024.